

**Molecular modelling and Invitro studies of the
therapeutic potential of *Ichnocarpus frutescens* and
*Hemidesmus indicus***



THESIS SUBMITTED IN PARTIAL FULFILLMENT
FOR THE AWARD OF DEGREE
DOCTOR OF PHILOSOPHY

By

Sonali Kumari

School of Biochemical Engineering
Indian Institute of Technology
(Banaras Hindu University)
Varanasi- 221005

CERTIFICATE

It is certified that the work contained in the thesis titled "**Molecular modelling and Invitro studies of the therapeutic potential of *Ichnocarpus frutescens* and *Hemidesmus indicus***" by **Sonali Kumari** has been carried out under my supervision and that this work has not been submitted elsewhere for a degree.

It is further certified that the student has fulfilled all the requirements of Comprehensive, Candidacy, RPEC, and SOTA for the award of a PhD degree.

Abha Mishra
29.8.25

Prof. Abha Mishra
(Supervisor)
School of Biochemical Engineering
Indian Institute of Technology
(Banaras Hindu University)
Varanasi – 221005, India

DECLARATION BY THE CANDIDATE

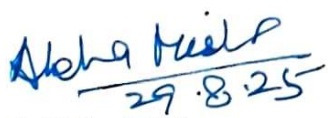
I, Sonali Kumari, certify that the work embodied in this thesis is my own bona fide work and carried out by me under the supervision of Prof. Abha Mishra from July 2019 to December 2024, at the "School of Biochemical Engineering", Indian Institute of Technology (Banaras Hindu University), Varanasi. The matter embodied in this thesis has not been submitted for the award of any other degree/diploma. I declare that I have faithfully acknowledged and given credit to the research workers wherever their works have been cited in my work in this thesis. I further declare that I have not willfully copied any other's work, paragraphs, text, data, results, etc., reported in journals, books, magazines, reports, dissertations, thesis, *etc.*, or available at websites, and have not included them in this thesis and have not cited them as my own work.

Date: 29/08/2025
Place: Varanasi



Signature of the Student
(Sonali Kumari)

CERTIFICATE BY THE SUPERVISOR(S)

It is certified that the above statement made by the student is correct to the best of my/our knowledge.


Prof. Abha Mishra
(Supervisor)
School of Biochemical Engineering
Indian Institute of Technology
(Banaras Hindu University)
Varanasi – 221005, India

PROFESSOR
Dr. ABHA MISHRA
SCHOOL OF BIOCHEMICAL ENGG.
INDIAN INSTITUTE OF TECHNOLOGY


Coordinator
School of Biochemical Engineering
Indian Institute of Technology
(Banaras Hindu University)
Varanasi – 221005, India
School of Biochemical Engg
भारतीय प्रौद्योगिकी संस्थान
Indian Institute of Technology
(कोशी) (Banaras Hindu University)
Varanasi-221005

COPYRIGHT TRANSFER CERTIFICATE

Title of the Thesis: "Molecular modelling and Invitro studies of the Therapeutic Potential of *Ichnocarpus frutescens* and *Hemidesmus indicus*"

Name of the Student: Sonali Kumari

Copyright Transfer

The undersigned hereby assigns to the Indian Institute of Technology (Banaras Hindu University), Varanasi, all rights under copyright that may exist in and for the above thesis submitted for the award of the "*Doctor of Philosophy (PhD)*".

Date: 29/08/2025

Place: Varanasi



Signature of the Student

(Sonali Kumari)

Note: However, the author may reproduce or authorize others to reproduce material extracted verbatim from the thesis or a derivative of the thesis for the author's personal use, provided that the source and the Institute's copyright notice are indicated.

ACKNOWLEDGEMENT

Through this page, I offer my salutation to the creator of this pious seat of learning, Bharat Ratna Mahamana Pt. Madan Mohan Malviya Ji.

It is indeed my proud privilege to express my deep sense of gratitude and indebtedness to my supervisor, **Prof. Abha Mishra**, Professor, School of Biochemical Engineering, Indian Institute of Technology (BHU), Varanasi, for their immense help, cooperation, and valuable guidance that they have extended to me for the successful completion of this investigation. I am grateful for their constant encouragement, sustained interest, and parental care throughout the research period.

I am obliged to express my sincere thanks to the present Coordinator, Dr. Pranjal Chandra, and former Coordinator Prof. Vikas Kumar Dubey, School of Biochemical Engineering, Indian Institute of Technology (BHU), for providing the necessary facilities and constant motivation throughout my research journey.

It is my privilege to express my thanks to all RPEC members, Prof. Siva Hemalatha, Department of Pharmaceutical Engineering and Technology, IIT (BHU), and Dr. Sanjay Kumar, School of Biochemical Engineering, IIT (BHU), for their appropriate suggestions and kind cooperation.

I am obliged to express my sincere thanks to all the faculty members of School of Biochemical Engineering, IIT (BHU), Prof. Pradeep Srivastava, Dr. Vishal Mishra, Dr. Abhishek Suresh Dhoble, Dr. Prodyut Dhar, Dr. Sumit Kumar Singh, Dr. Aditya Kumar Padhi, Dr. Rajendra Prasad and Dr. Sharon Mano Pappu J, for their support and encouragement.

I am obliged to express my sincere thanks to all the former faculty members, Prof. Subir Kundu, Prof. S. K. Srivastava, Prof. R. M. Banik, and Prof. Meera Debnath, School of Biochemical Engineering, IIT (BHU), for their guidance and encouragement.

I am grateful to Prof. Amit Singh, Professor in the Department of Pharmacology at the Institute of Medical Science, Banaras Hindu University, for guiding me throughout my PhD journey and keeping me motivated.

I also gratefully acknowledge the Council of Scientific and Industrial Research (CSIR), New Delhi, India, for the financial support in the form of a Junior Research Fellowship (JRF) and a Senior Research Fellowship (SRF).

I am also deeply thankful to all the non-teaching staff of the School of Biochemical Engineering, IIT (BHU), whose technical assistance was crucial to the smooth progress of my research.

My heartfelt thanks go to my dear lab mates. I would like to especially thank Dr. Aditi, Mr. Abhay, Mr. Arpit, Ms. Shruti, Ms. Aishwarya, Mr. Ravi, Mr. Ayush, Ms. Pooja, Dr. Alok, and Dr. Deepankar for their valuable support and encouragement towards the successful completion of my research work and for making the journey happy.

I gratefully acknowledge the late Shri Mahendra Pratap Singh for generously providing the plant samples essential to this research; his help made this work possible.

I also extend my sincere thanks to Dr. Kancharla Bhanukiran, Department of Pharmaceutical Engineering & Technology, IIT (BHU) Varanasi, for generous guidance and hands-on assistance with silica gel column chromatography setup, optimization, and troubleshooting.

I am deeply grateful to my friend, Ms. Darshna, whose unwavering support, from thoughtful advice and late-night pep talks to patient assistance with instrument operation and staying late to prepare plant samples, was invaluable.

I owe everything to my father, Dr. Brajesh Singh, and my mother, Shisham Singh, whose blessings and unshakeable faith have been my compass; their wisdom, quiet strength, and countless sacrifices, wrapped in daily prayers and unconditional love, carried me through the toughest and most tedious stretches of this journey. Without their support and motivation, I cannot even imagine my present position in life.

My deepest thanks to my husband, Dr. Ravi Saini, for being with me at every step of this journey, helping me in experiments, and for being joyful in every small win, whose love and encouragement steadied me whenever I felt overwhelmed and anchored me when the work became most demanding.

I am deeply grateful to my brother, Siddharth Chandan, my sister, Sonam Singh, and brother-in-law, Pushpendra Kumar, whose care, constant motivation, and ability to make me smile turned challenges into momentum and reminded me, again and again, that I never walked this path alone. I extend my love and gratitude to my beloved niece Preesha and nephew Yug, whose innocent laughter and endless curiosity have been a constant source of joy and inspiration.

In loving memory of my late grandparents, whose blessings and quiet strength have shaped who I am. I carry their love in every step of this journey, their voices steadying me when I falter, their prayers holding me when I feel alone. I dedicate this work to their cherished memory with gratitude that will never fade.

Lastly, all glory and thanks to Almighty God for the courage to begin, the patience to continue, and the grace to complete this work.

Table of Contents

Table of Contents	ix
List of Figures	xiv
List of Tables	xxxiii
List of Abbreviations	xxxvi
List of Symbols	xlii
PREFACE	xlv
Chapter 1: Introduction and Objectives	1
1.1 Introduction	1
1.2 Objectives	5
Chapter 2: Review of Literature	7
2.1. Diabetes	7
2.1.1 Types of Diabetes:	8
2.1.2 Physiopathology of Diabetes:	10
2.1.3 Management of Diabetes	12
2.1.4 Medicinal plants in the management of diabetes	15
2.1.5 Phytoconstituents in the Management of Diabetes	17
2.2 Cancer	19
2.2.1 Pathophysiology of Cancer	20
2.2.2 Natural Compounds with Anti-Cancer Properties	23
2.3 Plant Profile	27
2.3.1 <i>Hemidesmus indicus</i>	28
2.3.2 <i>Ichnocarpus frutescens</i>	35
Chapter 3: Extraction, purification and Characterization of Bioactive constituents from <i>Hemidesmus indicus</i> and <i>Ichnocarpus frutescens</i>	43
3.1 Introduction	43
3.2 Materials and Methods	45

3.2.1 Plant material and authentication	45
3.2.2 Solvent extraction	45
3.2.3 Preliminary qualitative analysis	46
3.2.4 Quantitative phytochemicals analysis	48
3.2.5 Elemental Analysis	49
3.2.6 HR-LCMS	50
3.2.7 Isolation of Bioactive Constituents	50
3.2.8 Characterization of Isolated Compounds	52
3.3 Results and Discussions	54
3.3.1 Extraction Yield Qualitative Analysis	54
3.3.2 Qualitative Analysis	56
3.3.3 Quantitative phytochemicals analysis	57
3.3.4 Carbon, Hydrogen and Nitrogen (CHN) analysis	59
3.3.5 Inductively Coupled Plasma Atomic Emission Spectroscopy (ICP-AES)	61
3.3.6 HR-LCMS	62
3.3.7 Chemical and structural properties of isolated compounds	66
3.4 Conclusion	74
Chapter 4: Evaluation of the antioxidant capacity of the <i>Hemidesmus indicus</i> and <i>Ichnocarpus frutescens</i> extracts and their phytoconstituents	77
4.1 Introduction	77
4.2 Materials and Methods	79
4.2.1 DPPH Free Radical Scavenging Assay	79
4.2.2 Ferric Reducing Antioxidant Power (FRAP) Assay	79
4.2.3 Drug-Likeness and ADMET Profiling	80
4.2.4 Computational Study	80
4.3 Results and Discussions	83

4.3.1 DPPH Assay	83
4.3.2 FRAP Assay	86
4.3.3 Drug-Likeness and ADMET Profiling	89
4.3.4 Computational Study	91
4.4 Conclusion	108
Chapter 5: Biological evaluation and computational studies of phytoconstituents as Antidiabetic potential	111
5.1 Introduction	111
5.2 Materials	114
5.2.1 Chemicals and Reagents	114
5.2.2 Cell Line and Culture Conditions	114
5.3 Methods	115
5.3.1 α -Amylase Inhibition Assay	115
5.3.2. α -Amylase Mode of inhibition (MOI) Assay	115
5.3.3 α -Glucosidase inhibitory assay	116
5.3.4 Mode of Inhibition (MOI) Assay for α -Glucosidase	117
5.3.5 Cell line study	118
5.3.6 Computational Study	121
5.4 Results and Discussions	124
5.4.1 α -Amylase Inhibition Assay	124
5.4.2 Mode of α -Amylase Inhibition Assay	128
5.4.3 α -Glucosidase Inhibition Assay	131
5.4.4 Mode of α -Glucosidase Inhibition Assay	136
5.4.5 Cell line study	139
5.4.6 Computational Study	148
5.5. Conclusion	164
Chapter 6: Biological evaluation and computational studies of phytoconstituents as anti-cancer potential.	167

6.1 Introduction	167
6.2 Materials	170
6.2.1 Chemicals and Reagents	170
6.2.2 Cell Line and Culture Conditions	170
6.3 Methods	171
6.3.1 Cytotoxicity Study	171
6.3.2 Annexin V Apoptosis Assay	171
6.3.3 Cell Cycle Analysis	172
6.3.4 Gene Expression Analysis	173
6.3.5 Computational Study	177
6.4 Results and Discussion	180
6.4.1 Cytotoxicity Study	180
6.4.2 Annexin V Apoptosis Assay	182
6.4.3 Cell Cycle Analysis	185
6.4.4 Gene Expression Analysis	188
6.4.5 Computational Study	196
6.5 Conclusions	223
Chapter 7: Synthesis of zinc oxide nanoparticles using <i>Hemidesmus indicus</i> and <i>Ichnocarpus frutescens</i> root extract and their therapeutic applications	227
7.1 Introduction	227
7.2 Material and Methods	229
7.2.1 Chemicals and Reagents	229
7.2.2 Synthesis of zinc oxide nanoparticles	229
7.2.3 ZnOxNP Characterization	230
7.2.4 Antioxidant Potential	232
7.2.5 Antidiabetic Assay	233
7.2.6 Anticancer Potential	234

7.3 Results and Discussion	236
7.3.1 ZnOxNP Characterization	236
7.3.2 Antioxidant Potential	249
7.3.3 Antidiabetic Assay	251
7.3.4 Anticancer Potential	254
7.4 Conclusions	264
Chapter 8: Conclusions and Summary	267
References	272
List of Publications	363

List of Figures

Figure 2.1:	Classification of Diabetes Mellitus.....	8
Figure 2.2:	Pathophysiology of Diabetes	10
Figure 2.3:	Overview of therapeutic approaches for managing Diabetes Mellitus.....	13
Figure 2.4:	Phytochemicals target multiple molecular mechanisms to regulate cancer development and progression.....	22
Figure 2.5:	Anticancer effects of natural phytochemicals through apoptosis induction, metastasis inhibition, autophagy promotion, and cell cycle control.	24
Figure 2.6:	Plant and root of <i>Hemidesmus indicus</i> (L.) R. Br. Ex Schult	29
Figure 2.7:	Stem, Leaves and Root of <i>Ichnocarpus frutescens</i> R. Br.	36
Figure 3.1:	Process of Isolation of Silychristin from <i>Hemidesmus indicus</i> and Hyperoside from <i>Ichnocarpus frutescens</i>	51
Figure 3.2:	Extractive Yield of <i>Hemidesmus indicus</i> and <i>Ichnocarpus frutescens</i> root in different solvents. Bars show mean±SD; n= 3 independent extractions per solvent per species. Statistics were performed in GraphPad Prism using a two-way ANOVA (factors: species × solvent) followed by Tukey’s multiple-comparisons post hoc test. Brackets indicate the pairwise comparisons tested. Significance: $P<0.05$ (*), $P<0.01$ (**), $P<0.001$ (***), $P<0.0001$ (****); ns= not significant ($P= NS$) (two-tailed, $\alpha= 0.05$)......	55

- Figure 3.3:** Total Phenolic Content (TPC) of *Hemidesmus indicus* and *Ichnocarpus frutescens* root in different solvent extracts. Bars show mean \pm SD; n = 3 independent extractions per solvent per species. Statistics were performed in GraphPad Prism using a two-way ANOVA (factors: species \times solvent) followed by Tukey's multiple-comparisons post hoc test. Brackets indicate the pairwise comparisons tested. Significance: $P < 0.05$ (*), $P < 0.01$ (**), $P < 0.001$ (***), $P < 0.0001$ (****); ns = not significant ($P = NS$) (two-tailed, $\alpha = 0.05$).....58
- Figure 3.4:** Total Flavonoid Content (TFC) of *Hemidesmus indicus* and *Ichnocarpus frutescens* root in different solvent extracts. Bars show mean \pm SD; n = 3 independent extractions per solvent per species. Statistics were performed in GraphPad Prism using a two-way ANOVA (factors: species \times solvent) followed by Tukey's multiple-comparisons post hoc test. Brackets indicate the pairwise comparisons tested. Significance: $P < 0.05$ (*), $P < 0.01$ (**), $P < 0.001$ (***), $P < 0.0001$ (****); ns = not significant ($P = NS$) (two-tailed, $\alpha = 0.05$).....59
- Figure 3.5:** CHN elemental analysis of methanolic root extract of (a) representing *Hemidesmus indicus* and (b) representing *Ichnocarpus frutescens*.....60
- Figure 3.6:** HR-LCMS Chromatogram of *Hemidesmus indicus* methanolic extract showing (A) positive and (B) negative electrospray ionization spectra.63

Figure 3.7:	HR-LCMS Chromatogram of <i>Ichnocarpus frutescens</i> methanol extract showing (A) positive and (B) negative electrospray ionization spectra.	63
Figure 3.8:	The structure of phytochemicals isolated from <i>Hemidesmus indicus</i> (Fig. A. Silychristin) and <i>Ichnocarpus frutescens</i> (Fig. B. Hyperoside)	66
Figure 3.9:	TLC image of <i>Ichnocarpus frutescens</i> (fig. A) and <i>Hemidesmus indicus</i> (fig. B). The standard is respective pure compounds for a reference run.	67
Figure 3.10:	HPLC Chromatogram of (A) Pure silychristin, showing a single peak at around 5.5 minutes; (B) Column eluate from <i>Hemidesmus indicus</i> , displaying a similar peak at around 5.5 minutes, representing silychristin present in the <i>Hemidesmus indicus</i>	69
Figure 3.11:	HPLC Chromatogram of (A) Pure hyperoside, showing a single peak at around 2.88 minutes; (B) Column eluate from <i>Ichnocarpus frutescens</i> , displaying a similar peak at around 2.88 minutes, representing hyperoside present in the <i>Ichnocarpus frutescens</i>	70
Figure 3.12:	¹ H NMR spectrum of hyperoside (column eluents from <i>Ichnocarpus frutescens</i>).....	71
Figure 3.13:	¹ H NMR spectrum of Silychristin (column eluents from <i>Hemidesmus indicus</i>).....	71

Figure 3.14: ^{13}C NMR spectrum of hyperoside (column eluents from <i>Ichnocarpus frutescens</i>)	72
Figure 3.15: ^{13}C NMR spectrum of Silychristin (column eluents from <i>Hemidesmus indicus</i>)	72
Figure 3.16: HRMS spectrum of silychristin (column eluents from <i>Hemidesmus indicus</i>) showing a prominent peak at an m/z value of 481.1168.....	73
Figure 3.17: HRMS spectrum for hyperoside (column eluents from <i>Ichnocarpus frutescens</i>), showing a prominent peak at an m/z value of 463.0972.....	73
Figure 4.1: DPPH free radical scavenging activity of various concentrations (5–30 $\mu\text{g/mL}$) of Ascorbic Acid, Hyperoside, Silychristin, <i>Hemidesmus indicus</i> (H.I.), and <i>Ichnocarpus frutescens</i> (I.F.). Bars show mean \pm SD; n = 3 independent replicates per concentration per treatment. Statistics were performed in GraphPad Prism using a two-way ANOVA with factors treatment \times concentration, followed by Tukey’s multiple-comparisons post hoc test. Brackets denote the pairwise comparisons evaluated at each concentration. Significance: $P < 0.05$ (*), $P < 0.01$ (**), $P < 0.001$ (***), $P < 0.0001$ (****); ns = not significant ($P = \text{NS}$) (two-tailed, $\alpha = 0.05$).....	84
Figure 4.2: The Ferric Reducing Antioxidant Power assay of various concentrations (20–120 $\mu\text{g/mL}$) of Ascorbic Acid, Hyperoside, Silychristin, <i>Hemidesmus indicus</i> (H.I.), and <i>Ichnocarpus</i>	

frutescens (I.F.). Bars show mean \pm SD; n = 3 independent replicates per concentration per treatment. Statistics were performed in GraphPad Prism using a two-way ANOVA with factors treatment \times concentration, followed by Tukey's multiple-comparisons post hoc test. Brackets denote the pairwise comparisons evaluated at each concentration. Significance: $P < 0.05$ (*), $P < 0.01$ (**), $P < 0.001$ (***), $P < 0.0001$ (****); ns = not significant ($P = NS$) (two-tailed, $\alpha = 0.05$)..... 87

Figure 4.3: 2D image showing the Molecular docking interactions of Xanthine Oxidase with Silychristin (1), Hyperoside (2), and Ascorbic Acid (3)..... 93

Figure 4.4: Root Mean Square Deviation profile of Xanthine Oxidase in its apo state (yellow) and complexed with ligands Hyperoside (blue), Silychristin (green), and Ascorbic Acid (red) over the 100 ns Molecular Dynamics simulation..... 96

Figure 4.5: Solvent Accessible Surface Area of Xanthine Oxidase when complexed with ligands Hyperoside (blue), Silychristin (green), and Ascorbic Acid (red) over the 100 ns Molecular Dynamics simulation. 97

Figure 4.6: Radius of Gyration profile of Xanthine Oxidase when complexed with ligands Hyperoside (blue), Silychristin (green), and Ascorbic Acid (red) over the 100 ns Molecular Dynamics simulation. 98

Figure 4.7:	Number of Hydrogen Bonds profile of Xanthine Oxidase when complexed with ligands Hyperoside (blue), Silychristin (green), and Ascorbic Acid (red) over the 100 ns Molecular Dynamics simulation.....	99
Figure 4.8:	Root Mean Square Fluctuation (RMSF) profiles of Xanthine Oxidase in its apo form and in complex with Ascorbic Acid, Silychristin, and Hyperoside.	101
Figure 4.9:	Per residue decomposition of Xanthine Oxidase showing binding contributions of individual amino acid residues with the ligands Ascorbic Acid (red), Silychristin (green) and Hyperoside (blue). ...	106
Figures 5.1:	Percentage of α -A inhibition potential by the root of <i>Hemidesmus indicus</i> . Bars show mean \pm SD; n = 3 independent replicates per concentration per solvent. Statistics were performed in GraphPad Prism using a two-way ANOVA (factors: solvent \times concentration) followed by Tukey's multiple-comparisons post hoc test. Brackets denote the pairwise comparisons evaluated at each concentration. Significance: $P < 0.05$ (*), $P < 0.01$ (**), $P < 0.001$ (***), $P < 0.0001$ (****); ns = not significant ($P = NS$) (two-tailed, $\alpha = 0.05$).	125
Figures 5.2:	Percentage of α -A inhibition potential by the root of <i>Ichnocarpus frutescens</i> . Bars show mean \pm SD; n = 3 independent replicates per concentration per solvent. Statistics were performed in GraphPad Prism using a two-way ANOVA (factors: solvent \times concentration) followed by Tukey's multiple-comparisons post	

hoc test. Brackets denote the pairwise comparisons evaluated at each concentration. Significance: $P < 0.05$ (*), $P < 0.01$ (**), $P < 0.001$ (***), $P < 0.0001$ (****); ns = not significant ($P = NS$) (two-tailed, $\alpha = 0.05$)..... 126

Figures 5.3: α -A inhibition percentage by the isolated phytochemicals hyperoside and silychristin, in comparison to the positive control, acarbose. Bars show mean \pm SD; n = 3 independent replicates per concentration per compound. Statistics were performed in GraphPad Prism using a two-way ANOVA (factors: compound \times concentration) followed by Tukey's multiple-comparisons post hoc test. Brackets indicate pairwise comparisons between compounds at each concentration. Significance: $P < 0.05$ (*), $P < 0.01$ (**), $P < 0.001$ (***), $P < 0.0001$ (****); ns = not significant ($P = NS$) (two-tailed, $\alpha = 0.05$)..... 127

Figure 5.4: Mode of inhibition of α -A by methanolic root extract of *Hemidesmus indicus* using Lineweaver Burk plot. 128

Figure 5.5: Mode of inhibition of α -A by methanolic root extract of *Ichnocarpus frutescens* using Lineweaver Burk plot. 129

Figure 5.6: Mode of inhibition of α -A by acarbose using Lineweaver Burk plot. 130

Figure 5.7: Mode of inhibition of α -A by hyperoside using Lineweaver Burk plot. 130

Figure 5.8: Mode of inhibition of α -A by silychristin using Lineweaver Burk plot. 131

Figures 5.9: Percentage of α -G inhibition potential by the root of *Hemidesmus indicus*. Bars show mean \pm SD; n = 3 independent replicates per concentration per solvent. Statistics were performed in GraphPad Prism using a two-way ANOVA (factors: solvent \times concentration), followed by Tukey's multiple-comparisons post hoc test. Brackets indicate pairwise comparisons at each concentration. Significance: $P < 0.05$ (*), $P < 0.01$ (**), $P < 0.001$ (***), $P < 0.0001$ (****); ns = not significant ($P = NS$) (two-tailed, $\alpha = 0.05$).133

Figures 5.10: Percentage of α -G inhibition potential by the root of *Ichnocarpus frutescens*. Bars show mean \pm SD; n = 3 independent replicates per concentration per solvent. Statistics were performed in GraphPad Prism using a two-way ANOVA (factors: solvent \times concentration), followed by Tukey's multiple-comparisons post hoc test. Brackets indicate pairwise comparisons at each concentration. Significance: $P < 0.05$ (*), $P < 0.01$ (**), $P < 0.001$ (***), $P < 0.0001$ (****); ns = not significant ($P = NS$) (two-tailed, $\alpha = 0.05$).134

Figures 5.11: α -G inhibition percentage by the isolated phytochemicals hyperoside and silychristin, in comparison to the positive control, acarbose. Bars show mean \pm SD; n = 3 independent replicates per concentration per compound. Statistics were performed in GraphPad Prism using a two-way ANOVA (factors: compound \times concentration) followed by Tukey's multiple-comparisons post hoc test. Brackets indicate pairwise comparisons between

compounds at each concentration. Significance: $P < 0.05$ (*), $P < 0.01$ (**), $P < 0.001$ (***), $P < 0.0001$ (****); ns = not significant ($P = NS$) (two-tailed, $\alpha = 0.05$)..... 135

Figure 5.12: Mode of inhibition of α -G by methanolic root extract of *Hemidesmus indicus* using Lineweaver Burk plot. 136

Figure 5.13: Mode of inhibition of α -G by methanolic root extract of *Ichnocarpus frutescens* using Lineweaver Burk plot. 137

Figure 5.14: Mode of inhibition of α -G by acarbose using Lineweaver Burk plot. 138

Figure 5.15: Mode of inhibition of α -G by hyperoside using Lineweaver Burk plot. 138

Figure 5.16: Mode of inhibition of α -G by silychristin using Lineweaver Burk plot. 138

Figure 5.17: 3T3-L1 preadipocytes, displaying spindle-shaped morphology before differentiation (Figure A), and fully differentiated 3T3-L1 adipocytes after exposure to differentiation medium, characterized by a rounded shape and accumulation of lipid droplets, indicating successful adipogenesis (Figure B). 140

Figure 5.18: Percentage viability of 3T3-L1 cells after 24-hour treatment with silychristin (Figure A) and hyperoside (Figure B). Untreated = vehicle control (set to ~100%). Bars show mean \pm SD; n = 3 independent experiments per concentration. Statistics were performed in GraphPad Prism using one-way ANOVA within

each compound, followed by Dunnett's multiple-comparisons test vs the untreated control. Significance: $P < 0.05$ (*), $P < 0.01$ (**), $P < 0.001$ (***), $P < 0.0001$ (****); ns = not significant ($P = NS$) (two-tailed, $\alpha = 0.05$).....142

Figure 5.19: 2-NBDG glucose uptake assay on 3T3-L1 cells. (A) Untreated control cells; (B) Cells treated with hyperoside; (C) Cells treated with silychristin; (D) Bar graph representing the mean fluorescence intensity (MFI) of 2-NBDG uptake, where both hyperoside and silychristin treatments significantly increase glucose uptake compared to the control, with silychristin showing the greatest effect.143

Figure 5.20: Invitro scratch wound healing assay of 3T3L1 cells at 0, 24, and 48 hours post-treatment with hyperoside and silychristin, compared to untreated control cells. Yellow outlines highlight the wound area at each time point, showing cell migration and wound closure over time. Scale bar: 200 μm146

Figure 5.21: Percentage of wound healing at 24 and 48 hours for control, hyperoside, and silychristin-treated 3T3L1 cells. Bars show mean \pm SD; n = 3 independent experiments per group and time point. Statistics were performed in GraphPad Prism using a two-way ANOVA (factors: treatment \times time) followed by Tukey's multiple-comparisons test. Asterisks denote differences vs control at the same time point; Significance: $P < 0.05$ (*), $P <$

0.01 (**), $P < 0.001$ (***), $P < 0.0001$ (****); ns = not significant
 ($P = NS$) (two-tailed, $\alpha = 0.05$)..... 148

Figure 5.22: 2D plots showing molecular interaction between binding-site residues of α -A protein with ligands..... 151

Figure 5.23: 2D plots showing molecular interaction between binding-site residues of α -G protein with ligands. 153

Figure 5.24: RMSD profile of α -A protein in their apo and complex state observed during simulation of 100 ns..... 157

Figure 5.25: RMSD profile of α -G protein in their apo and complex state observed during simulation of 100 ns..... 157

Figure 5.26: RMSF profile of α -A protein in their apo and complex state observed during simulation of 100 ns..... 158

Figure 5.27: RMSF profile of α -G protein in their apo and complex state observed during simulation of 100 ns..... 158

Figure 5.28: SASA value of α -A protein in their apo and complex state observed during simulation of 100 ns..... 159

Figure 5.29: SASA value of α -G protein in their apo and complex state observed during simulation of 100 ns..... 159

Figure 5.30: RoG value of α -A protein in their apo and complex state was observed during simulation of 100 ns..... 160

Figure 5.31: RoG value of α -G protein in their apo and complex state observed during simulation of 100 ns. 160

Figure 5.32: Hydrogen bond pattern of α -A protein complexes with Acarbose, Hyperoside and Silychristin observed during simulation of 100 ns.	162
Figure 5.33: Hydrogen bond pattern of α -G protein complexes with Acarbose, Hyperoside and Silychristin observed during simulation of 100 ns.	162
Figure 6.1: Percentage viability of A549 cell line after being treated with different concentrations of Hyperoside. and incubated at 37°C with 5% CO ₂ at 24 hrs. Untreated = vehicle control (set to ~100%). Bars show mean \pm SD; n = 3 independent experiments per concentration. Statistics were performed in GraphPad Prism using a one-way ANOVA across concentrations with Dunnett’s multiple-comparisons test vs the untreated control. Significance: $P < 0.05$ (*), $P < 0.01$ (**), $P < 0.001$ (***), $P < 0.0001$ (****); ns = not significant ($P = NS$) (two-tailed, $\alpha = 0.05$).	181
Figure 6.2: Percentage viability of A549 cell line after being treated with different concentrations of Silychristin and incubated at 37°C with 5% CO ₂ at 24 hrs. Untreated = vehicle control (set to ~100%). Bars show mean \pm SD; n = 3 independent experiments per concentration. Statistics were performed in GraphPad Prism using a one-way ANOVA across concentrations with Dunnett’s multiple-comparisons test vs the untreated control. Significance: $P < 0.05$ (*), $P < 0.01$ (**), $P < 0.001$ (***), $P < 0.0001$ (****); ns = not significant ($P = NS$) (two-tailed, $\alpha = 0.05$).	181

Figure 6.3: Apoptosis assay on A549 cell line. The plots display the distribution of live, early apoptotic, late apoptotic, and debris cell populations in untreated control cells and after treatment with Hyperoside and Silychristin..... 184

Figure 6.4: Cell cycle arrest analysis of A549 cells. The histograms depicted cell distribution across SubG1, G0/G1, S, and G2/M phases of the cell cycle, indicating the effect of cell cycle progression in control (untreated) and treated with Silychristin and hyperoside. 188

Figure 6.5: RNA integrity analysis on agarose gel. (A) Represents control (untreated) A549 cells, (B) shows hyperoside-treated, and (C) shows silychristin-treated A549 cells. It shows distinct bands corresponding to 28S rRNA, 18S rRNA, 5S rRNA, and mRNA. The clarity of the 28S and 18S bands indicates the quality of RNA in the samples. 189

Figure 6.6: Melt curve analysis showing the melting temperatures of PCR products, confirming amplification specificity. 193

Figure 6.7: Fold change in expression of apoptotic and cell cycle regulatory genes (p21, p53, Caspase-3, and Bcl-2) normalized to β -actin, using Quantitative Real-time PCR. 194

Figure 6.8: 2D plots showing molecular interaction between binding-site residues of AXL Receptor Tyrosine Kinase with ligands. 201

Figure 6.9: 2D plots showing molecular interaction between binding-site residues of Insulin-Receptor with ligands. 202

Figure 6.10: 2D plots showing molecular interaction between binding-site residues of PDGFR with ligands.....	203
Figure 6.11: 2D plots showing molecular interaction between binding-site residues of VEGFR with ligands.....	204
Figure 6.12: RMSD plots for the AXL, IR, PDGFR, and VEGFR receptors in their apo states (red) and when complexed with Silychristin (green), Hyperoside (blue), and standard inhibitors (yellow) over a 200 ns molecular dynamics simulation.	205
Figure 6.13: RMSF profiles for AXL, IR, PDGFR, and VEGFR receptors in their apo states (red) and when complexed with Silychristin (green), Hyperoside (blue), and standard inhibitors (yellow) during molecular dynamics simulations of 200 ns.....	209
Figure 6.14: Solvent Accessible Surface Area profiles for AXL, IR, PDGFR, and VEGFR receptors during a 200 ns molecular dynamics simulation when complexed with Silychristin (green), Hyperoside (blue), and standard inhibitors (yellow).....	211
Figure 6.15: Radius of Gyration (RoG) profiles for AXL, IR, PDGFR, and VEGFR receptors over a 200 ns molecular dynamics simulation in complex with Silychristin (green), Hyperoside (blue), and standard inhibitors (yellow)	213
Figure 6.16: Hydrogen Bond profiles of AXL, IR, PDGFR, and VEGFR receptors complexed with Silychristin (green), Hyperoside (blue), and standard inhibitors (yellow) over a 200 ns molecular dynamics simulation.....	215

Figure 6.17:	Per-residue energy decomposition analysis of the AXL, IR, PDGFR, and VEGFR receptors in complex with Silychristin (green), Hyperoside (blue), and standard inhibitors (yellow) over the last 20% of the molecular dynamics simulation trajectory.....	221
Figure 7.1:	UV-VIS Spectroscopy of HI ZnOxNP and IF ZnOxNP.	237
Figure 7.2:	Particle Size Distribution of HI ZnOxNP.	238
Figure 7.3:	Particle Size Distribution of IF ZnOxNP.....	238
Figure 7.4:	Zeta Potential of HI ZnOxNP and IF ZnOxNP.....	239
Figure 7.5:	FTIR Spectrum of HI ZnOxNP	241
Figure 7.6:	FTIR Spectrum of IF ZnOxNP	241
Figure 7.7:	SEM analysis of HI ZnOxNP.....	242
Figure 7.8:	SEM analysis of IF ZnOxNP.....	243
Figure 7.9:	EDS analysis of HI ZnOxNP.	245
Figure 7.10:	EDS analysis of IF ZnOxNP.....	246
Figure 7.11:	TEM images of HI ZnOxNP.....	247
Figure 7.12:	TEM images of IF ZnOxNP.....	248
Figure 7.13:	DPPH Assay of Ascorbic Acid, HI ZnOxNP and IF ZnOxNP at Varying Concentrations (5–30 µg/mL). Bars show mean ± SD; n = 3 independent replicates per concentration per treatment. Statistics were performed in GraphPad Prism using a two-way ANOVA (factors: treatment × concentration) followed by Tukey’s multiple-comparisons post hoc test. Brackets indicate pairwise	

comparisons between treatments at each concentration. Significance: $P < 0.05$ (*), $P < 0.01$ (**), $P < 0.001$ (***), $P < 0.0001$ (****); ns = not significant ($P = NS$) (two-tailed, $\alpha = 0.05$).249

Figure 7.14: FRAP Assay of Ascorbic Acid, HI ZnOxNP and IF ZnOxNP at Various Concentrations (20–120 $\mu\text{g/mL}$). Bars show mean \pm SD; $n = 3$ independent replicates per concentration per treatment. Statistics were performed in GraphPad Prism using a two-way ANOVA (factors: treatment \times concentration) followed by Tukey’s multiple-comparisons post hoc test. Brackets indicate pairwise comparisons between treatments at each concentration. Significance: $P < 0.05$ (*), $P < 0.01$ (**), $P < 0.001$ (***), $P < 0.0001$ (****); ns = not significant ($P = NS$) (two-tailed, $\alpha = 0.05$).251

Figure 7.15: α -A Inhibition Activity of HI ZnOxNP and IF ZnOxNP. Bars show mean \pm SD; $n = 3$ independent replicates per concentration per treatment. Statistics were performed in GraphPad Prism using a two-way ANOVA (factors: treatment \times concentration) followed by Tukey’s multiple-comparisons post hoc test. Brackets indicate HI vs IF comparisons at each concentration. Significance: $P < 0.05$ (*), $P < 0.01$ (**), $P < 0.001$ (***), $P < 0.0001$ (****); ns = not significant ($P = NS$) (two-tailed, $\alpha = 0.05$).252

Figure 7.16: α -G Inhibition Activity of HI ZnOxNP and IF ZnOxNP. Bars show mean \pm SD; $n = 3$ independent replicates per concentration

per treatment. Statistics were performed in GraphPad Prism using a two-way ANOVA (factors: treatment \times concentration) followed by Tukey's multiple-comparisons post hoc test. Brackets indicate HI vs IF comparisons at each concentration. Significance: $P < 0.05$ (*), $P < 0.01$ (**), $P < 0.001$ (***), $P < 0.0001$ (****); ns = not significant ($P = NS$) (two-tailed, $\alpha = 0.05$)..... 253

Figure 7.17: Percentage viability of A549 cell line after 24-hour treatment with *Hemidesmus indicus* root extract. The cells were treated with varying concentrations of *Hemidesmus indicus* extract and incubated at 37°C with 5% CO₂. Untreated = vehicle control (~100%). Bars show mean \pm SD; n = 3 independent experiments per concentration. Statistics were performed in GraphPad Prism using a one-way ANOVA across concentrations with Dunnett's multiple-comparisons test vs the untreated control. Significance: $P < 0.05$ (*), $P < 0.01$ (**), $P < 0.001$ (***), $P < 0.0001$ (****); ns = not significant ($P = NS$) (two-tailed, $\alpha = 0.05$)..... 255

Figure 7.18: Percentage viability of A549 cell line after 24-hour treatment with HI ZnOxNP. The cells were treated with varying concentrations of HI ZnOxNP and incubated at 37°C with 5% CO₂. Untreated = vehicle control (~100%). Bars show mean \pm SD; n = 3 independent experiments per concentration. Statistics were performed in GraphPad Prism using a one-way ANOVA across concentrations with Dunnett's multiple-comparisons test vs the untreated control. Significance: $P < 0.05$ (*), $P < 0.01$ (**), $P <$

0.001 (***), $P < 0.0001$ (****); ns= not significant ($P = NS$) (two-tailed, $\alpha = 0.05$).255

Figure 7.19: Percentage viability of A549 cell line after 24-hour treatment with *Ichnocarpus frutescens* extract. The cells were treated with varying concentrations of *Ichnocarpus frutescens* extract and incubated at 37°C with 5% CO₂. Untreated = vehicle control (~100%). Bars show mean ± SD; n = 3 independent experiments per concentration. Statistics were performed in GraphPad Prism using a one-way ANOVA across concentrations with Dunnett’s multiple-comparisons test vs the untreated control. Significance: $P < 0.05$ (*), $P < 0.01$ (**), $P < 0.001$ (***), $P < 0.0001$ (****); ns = not significant ($P = NS$) (two-tailed, $\alpha = 0.05$).256

Figure 7.20: Percentage viability of A549 cell line after 24-hour treatment with IF ZnOxNP. The cells were treated with varying concentrations of IF ZnOxNP and incubated at 37°C with 5% CO₂. Untreated = vehicle control (~100%). Bars show mean ± SD; n = 3 independent experiments per concentration. Statistics were performed in GraphPad Prism using a one-way ANOVA across concentrations with Dunnett’s multiple-comparisons test vs the untreated control. Significance: $P < 0.05$ (*), $P < 0.01$ (**), $P < 0.001$ (***), $P < 0.0001$ (****); ns = not significant ($P = NS$) (two-tailed, $\alpha = 0.05$).257

Figure 7.21: Flow cytometry analysis of apoptosis in the A549 lung cancer cell line. The plots display the distribution of live, early apoptotic, late

apoptotic, and necrotic cell populations in untreated control cells and those treated with *Hemidesmus indicus* extract (HI Extract), zinc oxide nanoparticles synthesized from *Hemidesmus indicus* extract (HI Zn NP), *Ichnocarpus frutescens* extract (IF Extract), and zinc oxide nanoparticles synthesized from *Ichnocarpus frutescens* extract (IF Zn NP). 259

Figure 7.22: Cell cycle arrest analysis of A549 cells. The histograms illustrate the distribution of cells across different phases of the cell cycle (SubG1, G0/G1, S, and G2/M), indicating the effect of cell cycle progression in control (untreated) A549 cells and treated with *Hemidesmus indicus* extract (HI Extract), zinc oxide nanoparticles synthesized from *Hemidesmus indicus* extract (HI Zn NP), *Ichnocarpus frutescens* extract (IF Extract), and zinc oxide nanoparticles synthesized from *Ichnocarpus frutescens* extract (IF Zn NP). 263

List of Tables

Table 2.1:	List of Medicinal plants with antidiabetic activity.....	16
Table 2.2:	Phytoconstituents in the Management of Diabetes.	17
Table 2.3:	Phytochemicals and Their Role in Cancer Therapy: Targets, Mechanisms of Action, and Cancer Types	24
Table 2.4:	Traditional uses of <i>Hemidesmus indicus</i> based on the different plant parts used.....	32
Table 2.5:	Pharmacological activity of chemical constituents of <i>Hemidesmus indicus</i>	33
Table 2.6:	Traditional uses of <i>Ichnocarpus frutescens</i> based on the different plant parts used.....	39
Table 2.7:	The pharmacological activity of chemical constituents of <i>Ichnocarpus frutescens</i>	42
Table 3.1:	Qualitative phytochemical analysis of <i>Hemidesmus indicus</i> and <i>Ichnocarpus frutescens</i> in different solvents.....	56
Table 3.2:	List of secondary metabolites of <i>H. indicus</i> from methanolic root extract.	64
Table 3.3:	Secondary metabolites of <i>Ichnocarpus frutescens</i> methanolic root extract using HR-LCMS technique.....	65
Table 4.1:	ADMET and toxicity profiles of hyperoside and silychristin.	90
Table 4.2:	MMGBSA profile analysis of the binding interactions between Xanthine Oxidase and the ligands Silychristin, Ascorbic Acid, and Hyperoside.....	104

Table 5.1:	IC ₅₀ values for the α -A inhibition of various extracts from <i>Hemidesmus indicus</i> and <i>Ichnocarpus frutescens</i> , as well as isolated phytochemicals (hyperoside and silychristin) and the positive control (acarbose).....	124
Table 5.2:	IC ₅₀ values for the α -G inhibition of various extracts from <i>Hemidesmus indicus</i> and <i>Ichnocarpus frutescens</i> , as well as isolated phytochemicals (hyperoside and silychristin) and the positive control (acarbose).....	132
Table 5.3:	Molecular docking interactions of Acarbose, Hyperoside, and Silychristin with α -A and α -G, showing varying binding affinities, and key residues involved in hydrogen bonding and hydrophobic interactions.....	149
Table 5.4:	MM/GBSA estimates of the binding free energy (Kcal/mol).....	163
Table 6.1:	Forward (F) and reverse (R) primer sequences, lengths, melting temperatures (T _m), and references used for Q-PCR analysis of gene expression of β -Actin, p21, p53, Caspase-3, and Bcl-2 in A549 cells.	175
Table 6.2:	Quantification of extracted RNA samples on NanoDrop for control, hyperoside-treated, and silychristin-treated samples.	190
Table 6.3:	CT values for the target genes Bcl-2, Caspase3, P21, and P53, along with the reference gene β -actin, across both control and treatment groups by Hyperoside and Silychristin.....	191

Table 6.4:	Molecular docking scores and interactions of Silychristin, Hyperoside, and standard inhibitors with AXL, IR, PDGFR, and VEGFR receptors, detailing the specific amino acid residues involved.....	197
Table 6.5:	MMGBSA profile analysis of the protein-ligand complexes for AXL, IR, PDGFR, and VEGFR over the last 20% of the simulation frames, with energy components presented in kcal/mol.....	218

List of Abbreviations

3T3-L1 - Mouse Embryonic Fibroblast Cell Line

Abs - Absorbance of sample

Ac - Absorbance of Control

ACTB - Beta-Actin (Housekeeping Gene)

AKT - Protein Kinase B

AL - Aluminum

ALL - Acute Lymphocytic Leukemia

AML - Acute Myeloid Leukemia

ATP - Adenosine Triphosphate

AXL - AXL Receptor Tyrosine Kinase

AXL - AXL Receptor Tyrosine Kinase

B.C. - Before Christ

BBB - Blood-Brain Barrier

Bcl-2 - B-Cell Lymphoma 2 (Anti-apoptotic Protein)

BE - Binding Energy

Ca - Calcium

Caspase-3 (CASP3) - Cysteine-Aspartic Acid Protease 3 (Apoptotic Gene)

CD3OD - Deuterated Methanol

CLL - Chronic Lymphocytic Leukemia

CML - Chronic Myeloid Leukemia

CNS - Central Nervous System

Ct - Cycle Threshold

Cu - Copper

CVD - Cardiovascular Disease

DKA - Diabetic Ketoacidosis

DLS - Dynamic Light Scattering

DMEM - Dulbecco's Modified Eagle Medium

DNA - Deoxyribonucleic Acid

DNase - Deoxyribonuclease

DPP-4 - Dipeptidyl Peptidase-4

DPPH - 2,2-Diphenyl-1-Picrylhydrazyl

EDS - Energy Dispersive Spectroscopy

EGFR - Epidermal Growth Factor Receptor

FBS - Fetal Bovine Serum

Fe - Iron

FITC - Fluorescein Isothiocyanate

FRAP - Ferric Reducing Antioxidant Power

FT-IR - Fourier-Transform Infrared Spectroscopy

g/mol - Grams per Mole

GA Runs - Genetic Algorithm Runs

GDM - Gestational Diabetes Mellitus

GLP-1 - Glucagon-like Peptide-1

GLUT-4 - Glucose Transporter Type 4

HER2 - Human Epidermal Growth Factor Receptor 2

HI ZnOxNP - *Hemidesmus Indicus* Zinc Oxide Nanoparticles

HPLC - High-Performance Liquid Chromatography

HR-LCMS - High-Resolution Liquid Chromatography-Mass Spectrometry

HR-MS / HRMS - High-Resolution Mass Spectrometry

IC₅₀ - Half-Maximal Inhibitory Concentration

IDF - International Diabetes Federation

IF ZnOxNP - *Ichnocarpus Frutescens* Zinc Oxide Nanoparticles

IR - Insulin Receptor

IV – Intravenous

kcal/mol - Kilocalories per mole (energy unit).

K_m - Michaelis-Menten Constant

LogP - Partition Coefficient

m/z - Mass-to-Charge Ratio

MAPK - Mitogen-Activated Protein Kinase

MD - Molecular Dynamics

MFI - Mean Fluorescence Intensity

Mg - Magnesium

mg/mL - Milligrams per Milliliter

mL - Milliliter

mM - Millimolar

MM/GBSA - Molecular Mechanics/Generalized Born Surface Area

mRNA - Messenger RNA

MS/MS - Tandem Mass Spectrometry

MTT - 3-(4,5-dimethylthiazol-2-yl)-2,5-diphenyltetrazolium bromide

Na - Sodium

NaCl - Sodium Chloride

nm - Nanometer

NMR - Nuclear Magnetic Resonance

NPT - Constant Number of Particles, Pressure, and Temperature

ns - Nanoseconds

NVT - Constant Number of Particles, Volume, and Temperature

OD - Optical Density

P - Phosphorus

p21 (CDKN1A) - Cyclin-Dependent Kinase Inhibitor 1A

p53 - Tumor Suppressor Gene

PBS - Phosphate-Buffered Saline

PDB - Protein Data Bank

PDBQT - Protein Data Bank Quaternion Translation Format

PDGFR - Platelet-Derived Growth Factor Receptor

PDI - Polydispersity Index

PI - Propidium Iodide

PSA - Polar Surface Area

qRT-PCR - Quantitative Real-Time Polymerase Chain Reaction

RMSD - Root Mean Square Deviation

RMSF - Root Mean Square Fluctuation

RNA - Ribonucleic Acid

RNase - Ribonuclease

RoG - Radius of Gyration

ROS - Reactive Oxygen Species

rpm - Revolutions per Minute

rRNA - Ribosomal RNA

RTK - Receptor Tyrosine Kinase

SAED - Selected Area Electron Diffraction

SASA - Solvent Accessible Surface Area

SDF - Structure Data File

SEM - Scanning Electron Microscopy

SGLT2 - Sodium-Glucose Cotransporter-2

Si - Silicon

SP - Standard Precision

SYBR - SYBR Green (Fluorescent Dye)

T1DM - Type 1 Diabetes Mellitus

T2DM - Type 2 Diabetes Mellitus

TEM - Transmission Electron Microscopy

TIP3P - Transferable Intermolecular Potential with 3 Points (Water Model)

TLC - Thin Layer Chromatography

TMS – Tetramethylsilane

U/mL - Units per milliliter (enzyme activity).

UV-VIS - Ultraviolet-Visible Spectroscopy

VEGFR - Vascular Endothelial Growth Factor Receptor

V_{max} - Maximum Reaction Rate

WBC - White Blood Cells

WHO - World Health Organization

XP - Extra Precision

Zn – Zinc

List of Symbols

Å - Angstrom (Unit of Length)

α -A - α -Amylase

α -G - α -Glucosidase

$\mu\text{g/mL}$ (μg) - Micrograms per milliliter (concentration unit).

% - Percentage (used for proportions, concentrations, and statistical data).

> - Greater than (used in comparisons).

+ - Addition or increase (used in reactions or combinations).

→ - Process or transition indicator.

/ - Denotes a ratio.

= - Equality or equivalence.

Fe^{3+} - Ferric ion (oxidized iron).

Fe^{2+} - Ferrous ion (reduced iron).

$^{\circ}\text{C}$ - Degrees Celsius (temperature).

pH - Measure of acidity or alkalinity.

$\times 100$ - Multiplication factor for percentage calculation.

ΔG - Change in free energy (binding or reaction energy).

\geq - Greater than or equal to.

\leq - Less than or equal to.

Å^2 - Square Ångström.

$\Delta\text{G}_{\text{bind}}$ - Binding free energy.

$\Delta E_{\text{Coulomb}}$ - Coulomb energy (electrostatic interaction energy).

ΔE_{Lipo} - Lipophilic energy (from hydrophobic interactions).

ΔE_{ele} - Electrostatic solvation energy (polar solvation effects).

ΔE_{vdW} - Van der Waals energy (non-covalent interaction energy).

2-NBDG - A fluorescent glucose analog.

μM - Micromolar (concentration unit).

μL - Microliter (volume unit).

V: Reaction velocity (rate of enzymatic reaction)

V_{max} : Maximum reaction velocity (enzyme saturation point)

K_{m} : Michaelis-Menten constant (substrate concentration at half V_{max})

ΔG_{total} - Total free energy

$\Delta G_{\text{protein}}$ - protein free energy

ΔG_{ligand} - ligand free energy

$T\Delta S$ - Entropic contribution to free energy.

m/z - Mass-to-charge ratio (mass spectrometry).

\pm - Plus-minus (standard deviation).

$p < 0.05$ - Statistical significance indicator.

$\times g$ - Gravitational force (centrifuge speed).

M - Molar concentration.

PREFACE

India is renowned for its rich heritage of herbal medicinal knowledge. In India, approximately 80% of the rural population uses medicinal herbs or indigenous medical systems. Among the numerous medicinal plants that originate from India, *Ichnocarpus frutescens* and *Hemidesmus indicus* are notable for their various traditional uses in treating a range of ailments. This research focuses on the extraction, purification, and characterization of bioactive compounds from root of *Hemidesmus indicus* and *Ichnocarpus frutescens*. The antidiabetic potential of these compounds was evaluated using *invitro* and *insilico* studies, targeting α -Amylase (α -A) and α -Glucosidase (α -G) inhibition. Additionally, *invitro* glucose uptake and wound healing assays were conducted to assess their therapeutic efficacy. The antioxidant potential of the plant extracts and isolated compounds was also investigated. The anticancer properties of the phytoconstituents were explored through biological and computational studies. Additionally, zinc oxide nanoparticles were also synthesized from the methanolic root extract of *Hemidesmus indicus* and *Ichnocarpus frutescens*, and their biological evaluation, including antioxidant, antidiabetic, and anticancer potentials, was conducted. Bioactive compounds silychristin was isolated from the roots of *Hemidesmus indicus* and hyperoside was isolated from *Ichnocarpus frutescens* using Column chromatography and were characterized using TLC, HPLC, ^1H and ^{13}C NMR, and HR-MS techniques. Hyperoside and silychristin exhibited significantly inhibitory effects against α -A and α -G than the standard drug, acarbose. The NBDG glucose uptake assay indicated that both compounds significantly enhanced glucose uptake compared to the control, with silychristin showing a more pronounced effect. DPPH assay, revealed that hyperoside exhibited the strongest antioxidant activity, while Silychristin and ascorbic acid showed similar antioxidant activities.

Biological evaluation and computational studies were conducted to assess the anticancer potential of phytoconstituents in the A549 lung cancer cell line. The studies included apoptosis, cell cycle analysis, and gene expression analysis. Silychristin and hyperoside exhibited 50% cell growth inhibition at concentrations of 96.46 $\mu\text{g/mL}$ and 74.61 $\mu\text{g/mL}$, respectively. The Annexin V apoptosis assay revealed that Hyperoside marked increase in late apoptotic and necrotic cell populations. Silychristin, while less potent, still induced apoptosis. Cell cycle analysis revealed distinct mechanisms of action for the two compounds. Hyperoside caused G2-M phase arrest, indicating interference with mitotic progression, while silychristin induced a strong G0-G1 phase arrest, effectively blocking DNA synthesis. Gene expression analysis indicated that the Bcl-2 gene was downregulated, whereas p21, p53, and Caspase-3 genes were upregulated compared to the housekeeping gene. Hyperoside treatment increased p21 expression 9-fold and silychristin 7-fold. For p53 expression, hyperoside caused a 2.4-fold increase, while silychristin led to a 3.7-fold increase. Caspase-3 expression was enhanced 4-fold by hyperoside and 6.7-fold by silychristin.

The zinc oxide nanoparticles using root extracts of *Hemidesmus indicus* (HI ZnOxNP) and *Ichnocarpus frutescens* (IF ZnOxNP) were also explored for their therapeutic applications, including antioxidant antidiabetic and anticancer potential. The synthesized nanoparticles were characterized through UV-VIS Spectroscopy, Particle Size Distribution and Zeta Potential Analysis, FT-IR Spectroscopy, Scanning Electron Microscopy (SEM), and Transmission Electron Microscopy (TEM). HI ZnOxNP exhibited superior free radical scavenging and ferric ion-reducing power compared to IF ZnOxNP. HI ZnOxNP demonstrated stronger inhibition of α -A, while IF ZnOxNP exhibited more potent inhibition of α -G. The anticancer studies on the A549 lung cancer cell line revealed that both HI ZnOxNP and IF ZnOxNP exhibit significantly higher

anticancer potential compared to their parent root extracts. Flow cytometry analysis demonstrated that HI ZnOxNP induced apoptosis more effectively than IF ZnOxNP, with a predominant late apoptotic response and minimal necrosis, highlighting its targeted cytotoxic mechanism. Both ZnOxNP also caused cell cycle arrest, with HI ZnOxNP inducing G0/G1 phase arrest and IF ZnOxNP exhibiting dual-phase inhibition, disrupting both DNA synthesis (S phase) and mitosis (G2/M phase). The combination of ZnOxNP with natural phytochemicals offers a novel strategy to improve the bioavailability, cellular uptake, and therapeutic efficacy of plant-derived compounds. These findings contribute to a deeper understanding of the therapeutic applications of *Hemidesmus indicus* and *Ichnocarpus frutescens*, suggesting their potential in treating type 2 diabetes, oxidative stress-related conditions, and cancer.

Keywords: *Hemidesmus indicus*, *Ichnocarpus frutescens*, *Bioactive Compounds*, *Cancer*, *Type 2 diabetes*.